

# **JGR** Solid Earth

#### RESEARCH ARTICLE

10.1029/2019JB017527

#### Key Points:

- Low Q<sub>P</sub>/Q<sub>S</sub> ratios (<1.5) are observed beneath the Lau back-arc spreading centers
- The low Q<sub>P</sub>/Q<sub>S</sub> ratios indicate bulk attenuation as high as 75% of the in situ shear attenuation
- High bulk attenuation coincides with partial melt in the Tonga-Lau mantle wedge

#### Supporting Information:

· Supporting Information S1

#### Correspondence to:

S. S. Wei, swei@msu.edu

#### Citation:

Wei, S. S., & Wiens, D. A. (2020). High bulk and shear attenuation due to partial melt in the Tonga-Lau back-arc mantle. Journal of Geophysical Research: Solid Earth, 125, e2019JB017527. https://doi.org/ 10.1029/2019JB017527

Received 10 FEB 2019 Accepted 7 DEC 2019 Accepted article online 11 DEC 2019

## High Bulk and Shear Attenuation Due to Partial Melt in the Tonga-Lau Back-arc Mantle

S. Shawn Wei<sup>1</sup> and Douglas A. Wiens<sup>2</sup>

Department of Earth and Environmental Sciences, Michigan State University, East Lansing, MI, USA, Department of Earth and Planetary Sciences, Washington University, St. Louis, MO, USA

**Abstract** Seismic attenuation measures energy loss during seismic wave propagation and quantifies the relaxation of rocks' elastic moduli. Abundant seismic studies have observed shear attenuation, but few have quantified bulk attenuation (bulk modulus relaxation), and these studies controversially locate finite bulk attenuation in different parts of the Earth, from the asthenosphere to the inner core. Here we present conclusive evidence localizing bulk attenuation to a specific region of the uppermost mantle. By analyzing amplitude spectral decay of P and S waves from Tonga earthquakes recorded at local seismic stations, we observe unusually low  $Q_P/Q_S$  ratios (<1.5) in the Tonga-Lau mantle wedge. All seismic raypaths with significant path-average bulk attenuation ( $Q_x^{-1} > 0.01$  or  $Q_x < 100$ ) are confined to the region immediately beneath the Lau back-arc spreading centers west of the Tonga Arc. Tomography results show that the highest bulk attenuation ( $Q_x^{-1} = 0.037 \pm 0.008$  or  $Q_x = 27.0 \pm 0.2$ ) is about 75% of the in situ shear attenuation. The observed high bulk attenuation anomalies coincide with an inferred zone of partial melting, suggesting that the causative mechanism involves either infinitesimal movement of melt through pores or changes in melt fraction in response to seismic waves.

#### 1. Introduction

#### 1.1. Seismic Bulk Attenuation

Seismic attenuation quantifies the energy loss of seismic waves during propagation, directly measuring the Earth's anelasticity that is a function of the physical properties of rocks, such as temperature, water content, and partial melting (Faul & Jackson, 2015; Takei, 2017). Measuring the Earth's seismic attenuation is important because attenuation provides a measure of conditions on the Earth's interior that is somewhat independent from seismic velocity (Dalton et al., 2008; Gung & Romanowicz, 2004). Knowledge of seismic attenuation is also necessary for determining earthquake magnitude and computing realistic synthetic seismograms (Romanowicz & Mitchell, 2015). Additionally, attenuation measurements are crucial for interpreting seismic velocity models because the dispersion caused by anelasticity may significantly change the observed seismic velocity (Karato, 1993).

In seismological studies, seismic attenuation is described quantitatively as the inverse of the quality factor Q. S-wave attenuation  $Q_S^{-1}$  is identical to the dissipation associated with shear modulus  $Q_\mu^{-1}$ , whereas P-wave attenuation  $Q_P^{-1}$  consists of dissipation associated with both shear modulus  $Q_\mu^{-1}$  and bulk modulus  $Q_\kappa^{-1}$ :

$$Q_p^{-1} = (1-L)Q_x^{-1} + LQ_u^{-1}$$
 (1)

$$Q_S^{-1} = Q_u^{-1}$$
 (2)

where  $L=(4V_S^2)/(3V_P^2)$  and  $V_P$  and  $V_S$  are P- and S-wave velocities, respectively (Anderson & Hart, 1978). Since global studies show that bulk attenuation  $Q_\kappa^{-1}$  is on average much less than shear attenuation  $Q_\mu^{-1}$  (e.g., Dziewoński & Anderson, 1981), it is commonly assumed that  $Q_\kappa^{-1}$  is negligible, giving  $Q_P/Q_S=2.25$  to 2.5 for the upper mantle.  $Q_P/Q_S$  ratios lower than 2.0 indicate the existence of significant bulk attenuation.

Shear attenuation has been extensively studied on global and regional scales, showing a significant variation through the mantle (Dalton et al., 2008; Eilon & Abers, 2017; Gung & Romanowicz, 2004; Nakajima et al., 2013; Pozgay et al., 2009; Rychert et al., 2008; Stachnik et al., 2004; Yang et al., 2007). In contrast, bulk attenuation is less well constrained, although there is agreement that finite bulk attenuation is required to simultaneously fit normal mode and surface wave data (Anderson & Hart, 1978). Whereas the

©2019. American Geophysical Union. All Rights Reserved.

WEI AND WIENS 1 of 16

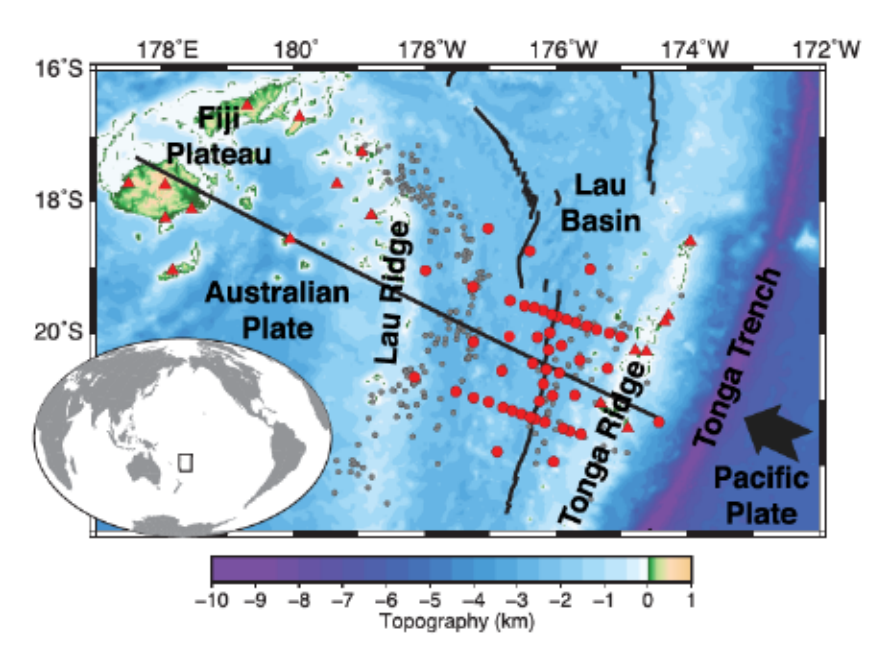


Figure 1. Map of the Tonga-Lau-Fiji region showing earthquakes and seismic stations. The Pacific plate subducts along the Tonga Trench from the southeast. Back-arc spreading centers are shown as black curves. The straight line represents the cross section shown in Figures 6–9. The gray dots indicate the locations of earthquakes with reliable  $t^*_P$  and  $t^*_S$  measurements that are used in this study. The red circles and triangles indicate ocean bottom seismographs and island-based seismic stations, respectively. The inset displays the study region on a global map.

preliminary reference Earth model (PREM; Dziewoński & Anderson, 1981) locates the bulk attenuation in the inner core, other global studies place it in the outer core (Anderson & Given, 1982), the lower mantle (Resovsky et al., 2005), the upper mantle (Sailor & Dziewoński, 1978), or more specifically in the asthenosphere (Durek & Ekström, 1995, 1996). Recent high-resolution studies of body wave attenuation in subduction zones show  $Q_P/Q_S$  ratios of greater than 2.0 in different mantle wedges, suggesting negligible bulk attenuation (Rychert et al., 2008; Stachnik et al., 2004). However, two studies report low  $Q_P/Q_S$  ratios (<2.0) beneath the Lau Basin (Roth et al., 1999) and the Mariana Trough (Pozgay et al., 2009), suggesting significant bulk attenuation in these mantle wedges, although the location of the high-bulk-attenuation region within the wedges could not be determined. Besides the studies of the Earth's core and mantle, seismic studies of shallow crustal attenuation often observe  $Q_P/Q_S$  smaller than 1.0, but attribute the low ratios to elastic scattering rather than intrinsic bulk attenuation (e.g., Hauksson & Shearer, 2006).

From the perspective of rock physics, it is generally agreed that grain boundary sliding is the predominant mechanism in the upper mantle that causes shear attenuation. This mechanism, however, cannot cause bulk attenuation (Faul & Jackson, 2015; Takei, 2017). Although some relaxation of the bulk modulus through a variety of microscopic mechanisms must take place within the Earth's wide mechanical relaxation spectrum, it is unknown whether the characteristic frequency falls into the seismic frequency band (Jackson, 2015). The physical mechanism and geological implication of bulk attenuation within the Earth are poorly understood, partly due to the lack of clearly defined seismic observations.

## 1.2. Tonga-Lau Subduction System

The Tonga subduction zone and the adjacent Lau back-arc basin, with an abundance of intermediate-depth and deep seismicity, provide a unique natural laboratory to study seismic attenuation in the upper mantle. This subduction system is known for the fastest convergence rate along the trench and the fastest total back-arc spreading rate of any trench/back-arc system in the world (Bevis et al., 1995). Intensive melting of the Tonga-Lau mantle wedge generates extensive magmatism along the Lau back-arc spreading centers and the Tofua arc (Kelley et al., 2006). The region of partial melting within the mantle wedge has been previously imaged as a low-velocity zone beneath the Lau back-arc basin west of the high-velocity Tonga slab (Conder & Wiens, 2006; Wei et al., 2015; Wei et al., 2016; Wiens et al., 2008). Additionally, previous studies of seismic

WEI AND WIENS 2 of 16



attenuation show a broad high-shear-attenuation zone beneath the Lau Basin, also indicating high temperature and partial melts in the mantle wedge (Barazangi & Isacks, 1971; Bowman, 1988; Roth et al., 1999). However, the existence of bulk attenuation is uncertain and not localized in those studies. Here we present new observations of  $Q_P^{-1}$  and  $Q_S^{-1}$  in the Tonga-Lau subduction system by analyzing seismic data from local land and ocean-bottom seismic stations (Figure 1) and show that significant bulk attenuation exists in the region of partial melting beneath the Lau Basin.

#### 2. Data and Methods

#### 2.1. Data Collection and Processing

We analyze seismic data recorded by the 2009–2010 Ridge2000 Lau Spreading Center Imaging project, which consisted of 49 ocean-bottom seismographs (OBSs) in the Lau Basin and 17 island-based seismic stations on the islands of Tonga and Fiji deployed for about 1 year (red symbols in Figure 1 and Table S1 in the supporting information). Each Woods Hole Oceanographic Institution OBS consisted of a Guralp CMG3T seismometer and a Quanterra Q330 datalogger, whereas the other OBSs from Lamont-Doherty Earth Observatory (LDEO) used modified Sercel L-4C seismometers and LDEO-designed recorders. Each island-based station consisted of a broadband three-component seismometer (Guralp CMG3T, Streckeisen STS-2 or Nanometrics Trillium 120 PA) and a Reftek 130-01 datalogger.

94,851 P arrivals and 14,772 S arrivals from 1,163 local earthquakes (December 2009 to October 2010; gray dots in Figure 1) were manually picked and were used to relocate the earthquakes (Wei et al., 2017). Events shallower than 50 km were excluded to eliminate waveforms with strong wave propagation effects associated with the Moho and near-source shallow structure. Seismograms were downsampled to 40 Hz and corrected for instrument response. Horizontal channels were rotated into a radial-transverse coordinate system based on previously determined OBS orientations (Zha et al., 2013).

#### 2.2. Determining t\*, Source Parameters, and Site Effects

We invert amplitude spectra of P and S waves from local intermediate-depth and deep earthquakes for the path-average attenuation operator  $t^* = t/Q$ , where t is the travel-time for each event-station pair. For the kth earthquake recorded at the jth station, the displacement spectrum  $A_{jk}(f_t)$  can be expressed as

$$A_{jk}(f_i) = \frac{C_{jk}M_{0k}e^{-\pi f_i^{1-\alpha}f_{0jk}}}{1 + (f_i/f_{ck})^2}$$
(3)

where  $C_{jk}$  is a constant factor for each event-station (k-j) pair accounting for geometric spreading, the free surface effect, and source radiation pattern;  $M_{0k}$  and  $f_{ck}$  are the seismic moment and the corner frequency for this event k, respectively;  $t^*_{0jk}$  is the attenuation factor at 1 Hz for event k and station j; and  $\alpha$  is a universal exponent characterizing the frequency dependence of attenuation as  $Q \propto f^{\alpha}$  (Anderson & Hough, 1984). Equation (3) is then solved with a nonnegative least squares algorithm for  $t^*_{0j}$  along each path as well as  $M_0$  and  $f_c$  for the event. This method has been previously used to study attenuation at several subduction zones (Pozgay et al., 2009; Rychert et al., 2008; Stachnik et al., 2004), and the detailed techniques are presented in another study of high-resolution P-wave attenuation tomography by Wei and Wiens (2018). Here we briefly introduce the key points and improvements.

Figure 2 shows an example of the  $t^*$  inversion for seismic waves from a 132-km-deep earthquake recorded at an OBS. We select a 5-s-long waveform starting 0.5 s before the arrival pick on the vertical channel as the P-wave signal, and the waveform with the same length immediately preceding the signal window as the P-wave noise. Both signal and noise spectra are calculated using a multitaper technique (Lees & Park, 1995), and the frequency band used for  $t^*$  inversion is automatically determined as a continuous frequency range in which the spectral signal-to-noise ratio > 2.0. We also discard frequencies lower than 0.05 Hz to avoid long-period noise in OBS data caused by ocean swell and local current and discard spectra with a frequency range smaller than 3 Hz for the  $t^*$  inversion. For each S wave, the data window and frequency band are determined in a similar way on the transverse component, with a window length of 8 s, a 0.5-s gap between the noise and signal windows, a lower spectral signal-to-noise ratio threshold of 1.8, and a minimum frequency range of 1 Hz (Figures 2b and 2d).

WEI AND WIENS 3 of 16

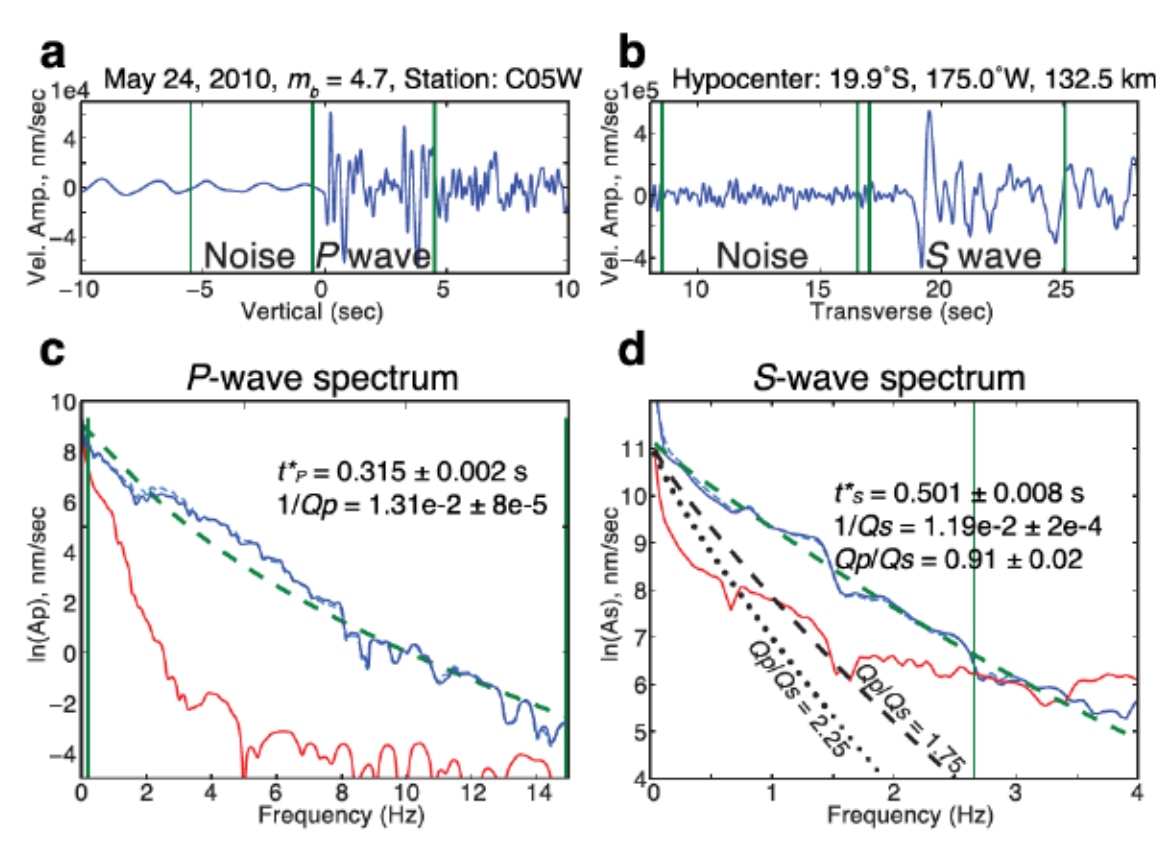


Figure 2. Example seismograms and  $t^*$  analysis. (a) P wave recorded on the vertical channel at ocean-bottom seismograph (OBS) C05W. The signal window starts 0.5 s before the P arrival pick to guarantee a full inclusion of the phase. The water-reflection phase (P wave reflected at the sea surface that is  $\sim$ 3 s after the direct P phase with a similar waveform) is observed at this OBS but has little influence on the measurements (see Figure S1 for details). (b) S wave recorded on the transverse component of the same OBS. The signal window starts 1 s before the S arrival pick. The green bars in (a) and (b) bound the windows of the signal and background noise. (c) Amplitude spectra of the P-wave signal (blue) and noise (red) of the waveform shown in (a). The dashed blue curve shows the P-wave spectrum after subtraction of site effects, which is almost identical to the original spectrum (blue solid curve). The green dashed curve shows the synthetic spectrum defined by the determined  $t^*P$  value of 0.31 s. The vertical green lines bound the frequency band used in the  $t^*$  inversion. (d) Spectra of the S-wave signal and noise showing the  $t^*S$  determination of 0.50 s, which together with the  $t^*P$  from (c) yields a  $Q_P/Q_S$  of 0.91. The black dashed curve indicates the predicted S-wave spectrum if  $Q_P/Q_S = 1.75$ , the regional average from Roth et al. (1999), and the black dotted curve shows the predicted spectrum if  $Q_P/Q_S = 2.25$  corresponding to no bulk attenuation.

We determine the best fitting  $f_c$  and  $t^*$  using a grid-search within a range of  $f_c$  values corresponding to stress drops varying from 0.5 to 20 MPa based on an assumption of a circular rupture and empirical relationships (Wei & Wiens, 2018). This strategy avoids any unrealistic values of  $f_c$  that might be determined by the  $t^*$  inversion because of the intrinsic trade-off between source ( $f_c$ ) and path terms ( $t^*$ ). In addition, we require  $f_{c(S)}$ , usually poorly constrained because of the limited S-wave frequency range, to be equal to  $f_{c(P)}$ . After trying different values of the frequency dependence exponent  $\alpha$ , we found that values between 0.2 and 0.4 provided the best fit (Wei & Wiens, 2018), so we assumed  $\alpha = 0.27$  in agreement with previous laboratory experiments (Faul & Jackson, 2015).  $t^*$  results with a poor fit to the spectra are discarded, and only event-station pairs with both reliable  $t^*_P$  and  $t^*_S$  measurements are used in the following analyses. The validation of these assumptions is discussed by Wei and Wiens (2018), and we will also show the impact of these assumptions on our results in section 3.2.

A water-reflection phase (P wave reflected at the seawater surface) can be sometimes observed in the OBS records ~3 s later than the direct P phase with an almost identical waveform (Figure 2a). Including this phase has little influence on the spectrum measurement due to the negligible P-wave attenuation in water (Figure S1 in the supporting information). Excluding the reflection using a shorter signal window may truncate the low-frequency components of some highly attenuated P waveforms, so we use a 5-s window even though it sometimes includes the water-reflection phase. We additionally correct for the frequency-dependent site effects by stacking residual spectra for each station and phase type (Stachnik et al., 2004;

WEI AND WIENS 4 of 16

Wei & Wiens, 2018). The site effects are generally small and show no systematic trends correlating to local geology (Figures S2 and S3). The final  $t^*$  measurements with the correction of site effects are used in the following analyses.

#### 2.3. Path-Average Attenuation and $Q_P/Q_S$

According to the definition,  $t^*$  can be converted to path-average attenuation  $Q^{-1} = t^*/t$  for P and S waves, and  $Q_P/Q_S = (t_P^*t_S)/(t_S^*t_P)$ , where  $t_P$  and  $t_S$  are P- and S-wave travel-times, respectively. Furthermore, path-average bulk attenuation  $Q_K^{-1}$  can be determined using equations (1) and (2):

$$\frac{1}{Q_{\kappa}} = \frac{1}{1 - L} \left( \frac{1}{Q_{P}} - \frac{L}{Q_{S}} \right) = \frac{1}{1 - L} \left( \frac{t_{P}^{\bullet}}{t_{P}} - L \frac{t_{S}^{\bullet}}{t_{S}} \right). \tag{4}$$

Since  $t_P$  and  $t_S$  are directly measured from the raw data, the path-average values are easily calculated, thus can provide general pattern of attenuation without the influence of tomography regularization.

In the example of Figure 2, the slopes of the P- and S-wave spectra determine  $t^*_P$  and  $t^*_S$ , respectively. The path-average  $Q_P/Q_S$  is  $0.91 \pm 0.02$ , much lower than 2.25 expected for only shear attenuation, indicating significant bulk attenuation along the raypath. Since  $t^*_P$  is better constrained than  $t^*_S$  due to the wider frequency band of the P wave, we check our results by calculating synthetic  $t^*_S$  with an assumed  $Q_P/Q_S$  and the well-constrained  $t^*_P$ , and then predicting the corresponding S-wave spectrum (black dashed and dotted curves in Figure 2d). It is impossible to fit the observed S-wave spectrum if we assume that the  $Q_P/Q_S$  is 1.75, which is the regional average found by Roth et al. (1999) or 2.25 corresponding to no bulk attenuation.

#### 2.4. Tomographic Inversion

We further solve for three-dimensional tomographic models of  $Q_P^{-1}$ ,  $Q_S^{-1}$ , and  $Q_P/Q_S$  using the  $t^*$  measurements obtained in section 2.2. The data are restricted to only event-station pairs with both reliable  $t^*_P$  and  $t^*_S$  measurements to avoid possible bias due to different sampling of P and S waves. Thus, the individual  $Q_P^{-1}$  and  $Q_S^{-1}$  models show lower resolution than those obtained with the entire dataset (Wei & Wiens, 2018), but in this way we obtain an unbiased estimate of the distribution of  $Q_P/Q_S$  ratios.

Similar to Wei and Wiens (2018), the tomographic inversion is solved as a linear problem as

$$t_i^* = \sum_j \frac{l_{ij}}{v_j} \frac{1}{Q_j} = G_{ij} m_j$$
 (5)

where  $t_i^*$  is the  $t_i^*$  measurement of the ith seismic ray, seismic velocity of the jth node  $(v_j)$ , and the path length for the ith ray around the jth node  $(l_{ij})$  together form the tomography kernel  $G_{ij}$ , and attenuation of the jth node  $(Q_j^{-1})$  is the model parameter  $m_j$ . We invert equation (5) separately for  $Q_P$  and  $Q_S$  using the  $t_P^*$  and  $t_S^*$  measurements, respectively. Seismic raypath lengths and travel-times are calculated by ray tracing with a pseudo-bending algorithm (Um & Thurber, 1987). We build a quasi-3-D velocity model for the ray tracing by projecting previously published 2-D  $P_T$ - and  $P_T$ - and  $P_T$ - wave velocity models in this region (Conder & Wiens, 2006; Wiens et al., 2008) parallel to the trench.

The tomographic inversion is performed using a maximum-likelihood linear inverse solution with a nonnegative least square algorithm (Menke, 2014). The model is parameterized with a grid of nodes spacing 77 km horizontally and 25–100 km vertically down to 300-km depth and a 1-D model from 350 to 700 km. An assumed uncertainty in theory of 0.03 s is input into the inversion based on previous experience (Rychert et al., 2008; Stachnik et al., 2004). Second-derivative smoothing and damping constraints are also imposed as a priori information. To choose the optimal inversion parameters, we conduct a series of inversion tests with synthetic data and different smoothing and damping coefficients and choose the values that result in the best recovery of the input models. We have also tested other synthetic models with a sparser grid spacing (Figure S4) and conclude that the current grid and inversion parameters are optimal. We do not try to densify the model grid because that will result in more model parameters than data points. The  $Q_P^{-1}$  and  $Q_S^{-1}$  models are independently obtained using the same damping and smoothing coefficients.

WEI AND WIENS 5 of 16

The  $Q_P/Q_S$  ratio can be obtained by simply dividing the two Q models obtained independently, but this result is subject to instability when  $Q_P^{-1}$  becomes very small. Therefore, we invert for the  $Q_P/Q_S$  model jointly using  $t^*_S$  measurements and the  $Q_P^{-1}$  model that is obtained from equation (5) with  $t^*_P$  data:

$$\left(t_{(S)}^*\right)_i = \sum_j \left[\left(\frac{l_S}{v_S}\right)_{ij} \left(\frac{1}{Q_P}\right)_j\right] \left(\frac{Q_P}{Q_S}\right)_j = G_{ij}m_j$$
 (6)

$$\mathbf{t}_{(S)}^* - \mathbf{G} \, \mathbf{m}_0 = \mathbf{G} \, (\mathbf{m} - \mathbf{m}_0) = \mathbf{G} \, \Delta \mathbf{m}$$
 (7)

where  $m_0$  is the reference model as  $Q_P/Q_S = 2.25$ . Compared to equation (5), the model parameter becomes  $(Q_P/Q_S)_j$  at the jth node. Because this equation solves for the deviation from a reference value, negative solutions are not problematic. We thus use a singular value decomposition (SVD) method (Menke, 2012) to invert equation (7) with the same grid of nodes. The SVD inversion separates the constrained and unconstrained model parameters so that the latter are damped to the reference value (2.25). The damping process is controlled by the number of singular values (p value), and a larger p value results in higher resolution but also higher model covariance (Figure S5). The optimal smoothing coefficient (2) and p value (90% of singular values) are determined based on tests with synthetic data. Model standard deviations are estimated by assuming model parameters are uncorrelated with each other.

Furthermore, we convert the  $Q_p^{-1}$  and  $Q_P/Q_S$  models to shear and bulk attenuation ( $Q_\mu^{-1}$  and  $Q_\kappa^{-1}$ ) based on the relationships between seismic attenuation and anelasticity of bulk and shear elastic moduli (equations (1) and (2)). This conversion also requires a  $V_P/V_S$  model, which is derived from the quasi-3-D velocity models that are used for raytracing. Although  $Q_\kappa^{-1}$  also depends on the  $V_P/V_S$  ratio, a moderate variation of  $V_P/V_S$  (0.2–0.3) may change  $Q_\kappa^{-1}$  by only 0.005 when  $Q_p^{-1}$  is higher than 0.01 and have little effect on  $Q_\kappa^{-1}$  when  $Q_p^{-1}$  is low (Figure S6). Therefore, the uncertainty of  $Q_\kappa^{-1}$  due to  $V_P/V_S$  is small compared to other uncertainties in the inversion, as discussed in the next section.

#### 3. Results

## 3.1. Path-Average Attenuation, $Q_P/Q_S$ , and $Q_\kappa$

952 earthquake-station paths show reliable  $t^*$  measurements for both P and S waves, with deep earthquakes being the predominant sources (Figure S7). The median uncertainties of  $t^*_P$ ,  $t^*_S$ , path-average  $Q_P^{-1}$ ,  $Q_S^{-1}$ , and  $Q_P/Q_S$  are 0.004 s, 0.016 s, 0.0005, 0.0004, and 0.1, respectively (Figure S8), which are comparable with that in previous studies in Alaska and Marianas (Pozgay et al., 2009; Stachnik et al., 2004). The observed S waves have a faster spectral decay with frequency than P waves, as illustrated by larger  $t^*_S$  values than  $t^*_P$  for all earthquakes (Figure 3a). However, this is mainly due to the longer S-wave travel-time rather than high  $Q_P/Q_S$  ratios, and path-average  $Q_S^{-1}$  is not always larger than  $Q_P^{-1}$  for individual measurements (Figure 3b). More intriguingly, path-average  $Q_P/Q_S$  ratios recorded at back-arc stations are generally around 1.0, whereas the ratios at other stations are systematically larger (Figure 3c).

Figure 4a shows all raypaths, color-coded by path-average  $Q_P/Q_S$  ratios, that have reliable  $t^*_P$  and  $t^*_S$  measurements. We additionally estimate the mean value of path-average  $Q_P/Q_S$  ratios from all events shallower than 300 km (Figure 5a) and deeper than 300 km (Figure 5b) recorded at each station. Most raypaths in the back-arc mantle are characterized by low  $Q_P/Q_S$  ratios (0.7–1.5), whereas raypaths sampling the Tonga slab and the mantle beneath the Fiji Plateau have  $Q_P/Q_S$  ratios of 1.7–2.4, as expected if bulk attenuation is very low or absent (Figures 3c and 4a). Figures 3–5 also show that the low  $Q_P/Q_S$  ratios in the Lau Basin do not correlate with event depth. This, along with the fact that the low  $Q_P/Q_S$  ratios are observed for a wide variety of source and station locations, shows that the ratios are not due to wave propagation effects along particular paths. The results also indicate that the low  $Q_P/Q_S$  ratio measurements are controlled by the uppermost mantle attenuation structure, since the low  $Q_P/Q_S$  ratios are also observed for intermediate depth earthquakes that sample only the upper 150 km. Since the highest attenuation is observed in the uppermost mantle (e.g., Wei & Wiens, 2018), the path-average  $Q_P/Q_S$  ratios will be weighted towards the upper mantle values.

We further calculate path-average bulk attenuation  $Q_{\kappa}^{-1}$  based on equation (4) and  $Q_P/Q_S$  ratios. The resulting path-average  $Q_{\kappa}^{-1}$  can be as high as 0.02, and raypaths with high bulk attenuation ( $Q_{\kappa}^{-1} > 0.01$ ) are all

WEI AND WIENS 6 of 16

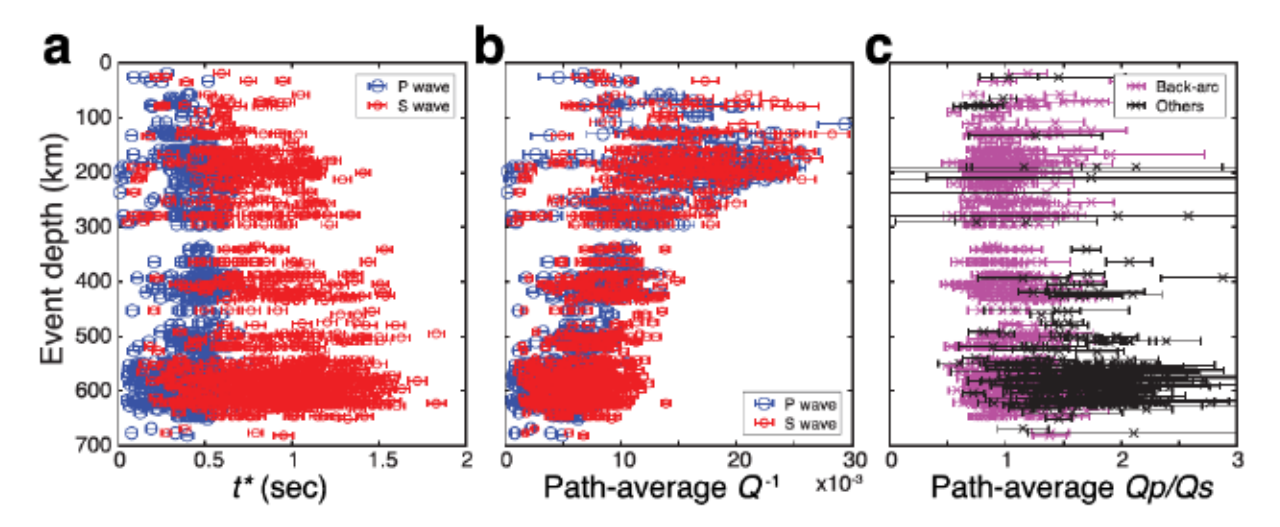


Figure 3.  $t^*_P$  and  $t^*_S$  determinations from event-station pairs providing high-quality measurements of both. (a)  $t^*$  measurements versus earthquake depth for P (blue) and S (red) waves. Each error bar indicates the  $t^*$  uncertainty as a sum of the inversion model standard deviation and an assumed systematic uncertainty (0.03 s). (b) Path-average attenuation  $(Q^{-1} = t^*/t)$ , where t is the travel-time calculated from the observed phase arrival times) versus earthquake depth for P (blue) and S (red) waves. The path-average attenuation peaks at 100- to 200-km depths, suggesting that the high-attenuation region is confined to the upper 200 km. The error bars indicate the uncertainties of the path-average attenuation assuming an uncertainty of 0.5 s in P-wave travel-time and an uncertainty of 1 s for S wave. (c) Path-average  $Q_P/Q_S$  ratio versus earthquake depth. The magenta crosses indicate path-average  $Q_P/Q_S$  ratios recorded at back-arc stations, showing low  $Q_P/Q_S$  ratios (0.7–1.5) beneath the Lau Basin. The black crosses show path-average  $Q_P/Q_S$  ratios recorded at other stations. The error bars indicate uncertainties of path-average  $Q_P/Q_S$  based on the uncertainties shown in (b).

confined in the mantle wedge beneath the Lau back-arc basin, whereas other raypaths show little bulk attenuation (Figure 5b).

## 3.2. Influence of $t^*$ -Inversion Assumptions on $Q_P/Q_S$

Here we examine the assumptions used in the  $t^*$  inversion and their possible effects on the  $Q_P/Q_S$  ratio determination. Q is commonly assumed to have a modest frequency dependence in the seismic band, quantified by the exponent  $\alpha$  (e.g., Flanagan & Wiens, 1998; Romanowicz & Mitchell, 2015). Since  $t^*_P$  and  $t^*_S$  are measured at overlapping but somewhat different frequency bands due to low signal-to-noise ratio for S waves at higher frequencies, an incorrect  $\alpha$  value could bias the  $Q_P/Q_S$  ratio, because  $\frac{Q_P}{Q_S} \propto \frac{f_S}{f_P} = \frac{f_{SS}}{f_{SP}} \left(\frac{f_P}{f_S}\right)^{\alpha}$ , where  $t^*_{OP}$  and  $t^*_{OS}$  are the attenuation factors at 1 Hz for P and S waves, respectively. If we assume the central P-wave frequency is consistently 4 times higher than S-wave frequency (i.e.,  $f_P/f_S = 4$ ), large  $\alpha$  values of about 0.7–0.8 will yield  $Q_P/Q_S$  ratios that are larger by a factor of 1.8 to 2. Thus, the extremely low observed  $Q_P/Q_S$  ratios (<1.5) and their interpretation in terms of bulk attenuation can be avoided by assuming very strong frequency dependence of attenuation (high  $\alpha$  values). However, there is no evidence for such a strong frequency dependence of seismic attenuation from either a seismological or experimental perspective. With the Lau dataset, an  $\alpha$  of about 0.27 provides the best fit (Wei & Wiens, 2018) and is consistent with laboratory results for high temperature subsolidus olivine (e.g., Faul & Jackson, 2015). For a more realistic case, an increase of  $\alpha$  from 0.27 to 0.4 can increase the derived  $Q_P/Q_S$  ratio by a factor of only 1.1–1.2.

It is also worthwhile to discuss the potential bias caused by the source spectrum. Although we assume  $f_{c(S)} = f_{c(P)}$  for the  $t^*_S$  inversion, some previous studies (e.g. Pozgay et al., 2009) used  $f_{c(S)} = f_{c(P)}/1.5$  based on a circular rupture model (Madariaga, 1976). However, this alternative relationship of corner frequency will result in smaller  $t^*_S$  measurements, and thus even smaller  $Q_P/Q_S$  ratios compared to the current results, although the effects will be minor. Therefore, the possible bias due to S-wave corner frequency, if it exists, cannot explain the observed low  $Q_P/Q_S$  ratios, and should be excluded.

In order to test the validity of these assumptions, we also conduct  $t^*$ -inversions for the entire dataset with other possible values (Figures S9–S11). These include (1) a fixed  $f_{c(P)}$  determined by a fixed stress drop as 5, 10, or 20 MPa, (2) assuming  $f_{c(S)} = f_{c(P)}/1.5$  according to a circular rupture model (Madariaga, 1976), and (3) a frequency dependence exponent ( $\alpha$ ) value varying from 0 to 0.6. The average misfits of the  $t^*$  inversions for all these various assumptions suggest that a grid search of  $f_{c(P)}$ , requiring  $f_{c(S)} = f_{c(P)}$ , and  $\alpha = 0.27$ 

WEI AND WIENS 7 of 16

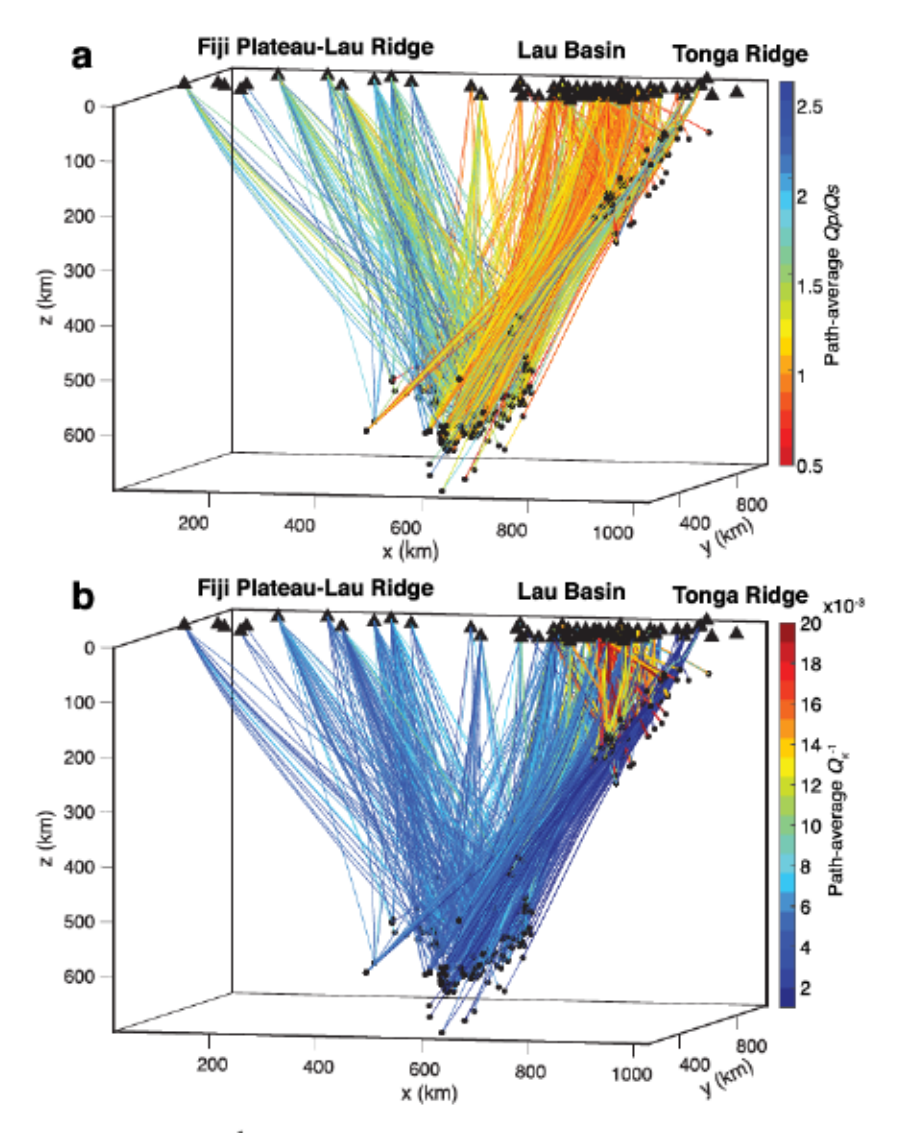


Figure 4. Path-average  $Q_P/Q_S$  and bulk attenuation  $Q_{\kappa}^{-1}$ . (a) 3-D image of P-wave raypaths color-coded by path-average  $Q_P/Q_S$  along each source-station pair. S-wave raypaths are slightly different but the differences are negligible at the scale of this figure. The black dots indicate the locations of earthquakes used in this study, and the black triangles on the top show seismic station locations. (b) Similar 3-D image of raypaths color-coded by path-average  $Q_{\kappa}^{-1}$  along each path. Raypaths with significant bulk attenuation ( $Q_{\kappa}^{-1} > 0.01$ ) are highlighted with bold curves and warm colors. Although raypaths with low  $Q_P/Q_S$  ratios can extend to 600-km depth, raypaths with high bulk attenuation are confined in the upper 200 km. This is because shear attenuation is low beneath 200-km depth.

are the strategies that provide the best fit to the data (Wei & Wiens, 2018). Furthermore, since all  $t^*$  results with poor fits are discarded, the final number of reliable  $t^*$  measurements is also indicative of the validity of the assumptions. For instance, there are much fewer acceptable  $t^*$  measurements for  $\alpha > 0.4$ , suggesting that these values on average provide a poor fit to the data. Nevertheless, all results show a large number of event-station pairs with path-average  $Q_P/Q_S$  ratios smaller than 1.5.

#### 3.3. Tomographic Results

Figure 6 shows the  $Q_P^{-1}$  and  $Q_S^{-1}$  tomography images for independent inversions based on equation (5), using 952 reliable  $t^*$  measurements for both P and S waves. Synthetic tests shown in Figure 7 illustrate the resolution and robustness of all models. The input models for  $Q_P^{-1}$  and  $Q_S^{-1}$  are designed to represent the model resolution length, whereas the input model for  $Q_P/Q_S$  is designed to represent the final model shown in Figure 8. More checkerboard tests shown in Figure S4 confirm that the current grid spacing and inversion parameters are optimal. Note that the path coverage for  $Q_P^{-1}$  and  $Q_S^{-1}$  are identical, so the images provide identical resolution.

WEI AND WIENS 8 of 16

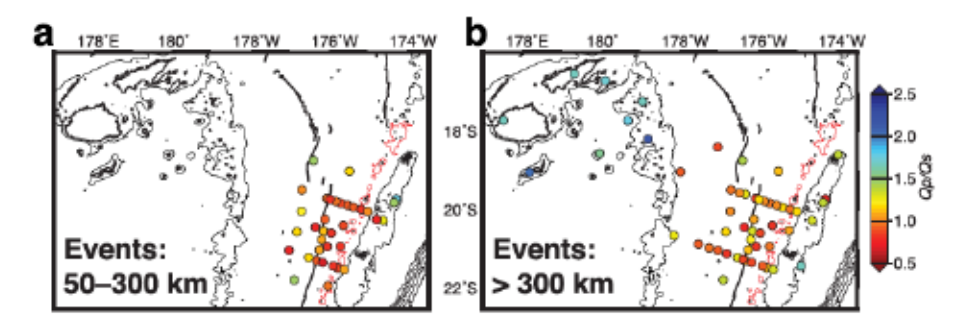


Figure 5. Mean value of the path-average  $Q_P/Q_S$  measurements at each station for (a) events with depth between 50–300 km and (b) events deeper than 300 km. Only stations with more than two measurements are plotted. Shallower events generally do not have  $Q_S$  measurements for the westernmost stations. Bathymetric contours of 1, 7, 8, 9, and 10 km are shown to highlight the tectonic features, with red contours denoting the Tofua volcanic arc. Coastlines and the back-arc spreading center are shown as bold dark lines. Most of the back-arc and arc stations are characterized by low  $Q_P/Q_S$  ratios, whereas most of the fore-arc and Fiji Plateau stations show higher  $Q_P/Q_S$  ratios.

High attenuation anomalies are located beneath the Lau back-arc basin, consistent with a higher-resolution  $Q_P$  model in this region based on more than 10,000  $t^*_P$  measurements (Wei & Wiens, 2018). Because the data are dominated by near-vertical raypaths from deep earthquakes (Figure S7), the structure may be smoothed vertically as shown by the checkerboard tests (Figure 7). This issue is more problematic for the structure beneath Fiji, as no S waves along near-horizontal raypaths can be observed at the Fijian stations. As a consequence, the depth of the high attenuation beneath the Fiji Plateau is poorly resolved and should likely be somewhat deeper as indicated by the higher-resolution  $Q_P^{-1}$  model (Wei & Wiens, 2018).

The  $Q_P^{-1}$  model shown in Figure 6a and the  $t^*_S$  measurements are used to jointly invert for a  $Q_P/Q_S$  model based on equations (6) and (7). The model resolution is highest beneath the back-arc basin (Figure 7i) where the standard deviation of  $Q_P/Q_S$  is generally less than 0.1 (Figure 7j). The results (Figure 8) show low  $Q_P/Q_S$  ratios in the mantle wedge, with the minimum values located in the upper 150 km of the mantle beneath the Lau back-arc basin. In contrast, the ratios beneath Fiji are about 1.8–2.0, relatively close to the expected 2.25 for attenuation purely in shear. These results are generally consistent with Roth et al. (1999), who determined an average  $Q_P/Q_S$  ratio of 1.75 for the entire region using a different method at slightly different frequencies and who had a higher percentage of observations from the Fiji plateau.

It is worthwhile to note that caution needs to be taken when interpreting small-scale anomalies of  $Q_P/Q_S$  and bulk attenuation in the next step. For instance, the  $Q_P/Q_S$  ratio beneath the Lau back-arc spreading centers at 25-km depth is higher (1.54  $\pm$  0.10) than at 100-km depth (0.66  $\pm$  0.08). The resolution tests (Figure 7) indicate that the  $Q_P/Q_S$  structure is not well resolved on a length and depth scale of <50 km, and the 25-km depth values may be biased by sampling the thin lithosphere. Nevertheless, since we use only raypaths with both  $t^*_P$  and  $t^*_S$  measurements, the potential bias due to the lack of S-wave observation has been minimized, so that the general pattern of  $Q_P/Q_S$  ratios should be reliable.

Shear and bulk attenuation models are further calculated based on equations (1) and (2) and the quasi-3D velocity model (Figure 9). Uncertainties of  $Q_{\kappa}^{-1}$  are estimated by propagating errors of  $Q_P$ ,  $Q_P/Q_S$ , and  $V_P/V_S$ . We assume an error of  $\pm$  0.1 as the upper bound of  $V_P/V_S$  uncertainty because a previous tomography image in this region (Figure 7 of Conder & Wiens, 2006) shows that  $V_P/V_S$  only varies from -0.1 to 0.1 throughout the entire subduction zone. The highest shear and bulk attenuation anomalies ( $Q_{\mu}^{-1} = 0.047 \pm 0.001$  and  $Q_{\kappa}^{-1} = 0.037 \pm 0.008$ ) are located beneath the back-arc spreading centers, giving a ratio of bulk to shear attenuation  $Q_u/Q_{\kappa}$  of  $\sim$ 0.75.

In sum, raypath-average results (Figures 4 and 5) are more robust due to the fewer assumptions but have low spatial resolution, whereas tomography results (Figures 8 and 9) can locate  $Q_P/Q_S$  and  $Q_\kappa^{-1}$  anomalies but depend on the velocity models as well as tomographic inversion parameters. Nevertheless, they all show unusually low  $Q_P/Q_S$  ratios and significant bulk attenuation in the mantle wedge immediately beneath the Lau back-arc spreading centers.

WEI AND WIENS 9 of 16

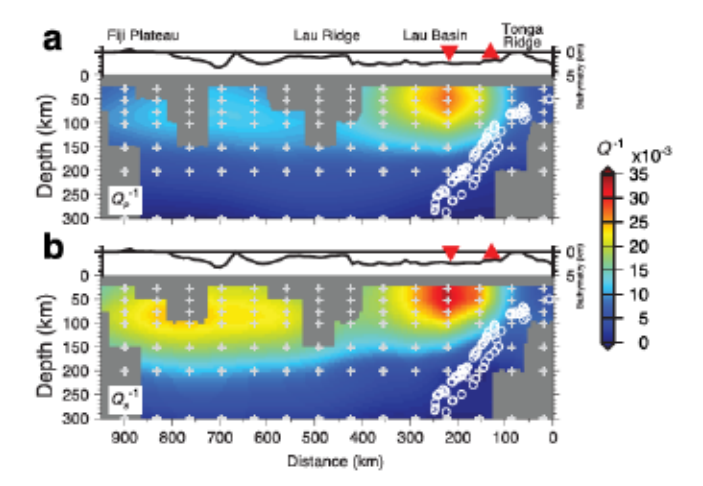


Figure 6.  $Q_P^{-1}$  and  $Q_S^{-1}$  tomographic models obtained by inverting equation (5) independently for P- and S-wave data. (a) Cross section of P-wave attenuation  $Q_P^{-1}$  structure. Regions with low raypath coverage (hit count lower than 10) are masked with gray. The cross-section location is shown as the straight line in Figure 1, roughly representing a 100-km wide vertical profile given the resolution tests. Topography and bathymetry are plotted above the images with a 10-time vertical exaggeration. The red triangles and red inverted triangles represent the volcanic arc and the back-arc spreading center, respectively. The white circles indicate the relocated intermediate-depth earthquakes less than 55 km away from the cross section (Wei et al., 2017) delineating the Tonga slab. The light gray crosses indicate the nodes used in tomographic inversion. (b) Similar cross section of S-wave attenuation  $Q_S^{-1}$ . The depth of the high attenuation zone beneath the Fiji Plateau is poorly resolved due to limited vertical resolution and probably should be somewhat deeper as discussed in the text.

## 4. Discussion

## Effects of Seismic Scattering on Q and Q<sub>P</sub>/Q<sub>S</sub>

Before discussing the implications of high bulk attenuation, it is necessary to distinguish intrinsic (anelastic) attenuation from effects of seismic scattering, which also dissipates seismic energy but in elastic ways. As high-frequency body waves propagate in an inhomogeneous media, they are reflected or refracted at small-scale scatterers, causing energy loss due to scattering, which is often described as scattering attenuation. Since P-to-S conversion is more efficient than S-to-P conversion at the scatterers, the scattering attenuation of P waves is usually larger than that of S waves, leading to a small  $Q_P/Q_S$  ratio (Sato et al., 2012). Therefore, the low  $Q_B/Q_S$  ratios observed in the crust are usually attributed to scattering due to fractures and cracks (e.g., Hauksson & Shearer, 2006). However, the effects of seismic scattering in the mantle wedge are generally considered to be negligible due to the lack of obvious scattering heterogeneities and the lowerfrequency data used for the inversion (Rychert et al., 2008; Stachnik et al., 2004). Additionally, scattering attenuation in the lithosphere is found to be highly frequency-dependent ( $\alpha = 0.7$ ; Sato, 1990), which is contrary to our results that provide the best data fit for  $\alpha = 0.2$ –0.3 (Wei & Wiens, 2018). A recent study of mantle heterogeneity (Mancinelli et al., 2016) suggests that the frequency dependence of scattering attenuation in the upper mantle is smaller than previously thought, giving an  $\alpha$  value of 0.1 (equivalent to  $\kappa = 0.05$  in their parameterization). But scattering attenuation predicted by that study is 1 order of magnitude weaker than the attenuation observed beneath the Lau Basin.

To further investigate the possibility of scattering attenuation, we use the statistical approach of Mancinelli et al. (2016) to predict scattering attenuation and then compare the results with the Lau Basin measurements. Spectral characteristics of heterogeneity are conveniently described with a statistical model: an ensemble of random media that have the same autocorrelation function (ACF). Here we assume that the media heterogeneity can be statistically parameterized with a von Kármán ACF, which is controlled by correlation length a, velocity perturbation  $\varepsilon$ , and order  $\kappa$ . Then the scattering attenuation can be calculated based on the travel-time corrected Born approximation (Sato, 1984; Sato et al., 2012). The peak amplitude of scattering attenuation is primarily controlled by  $\varepsilon$ , whereas a controls the peak frequency, and  $\kappa$  determines the frequency dependence at high frequencies.

WEI AND WIENS 10 of 16

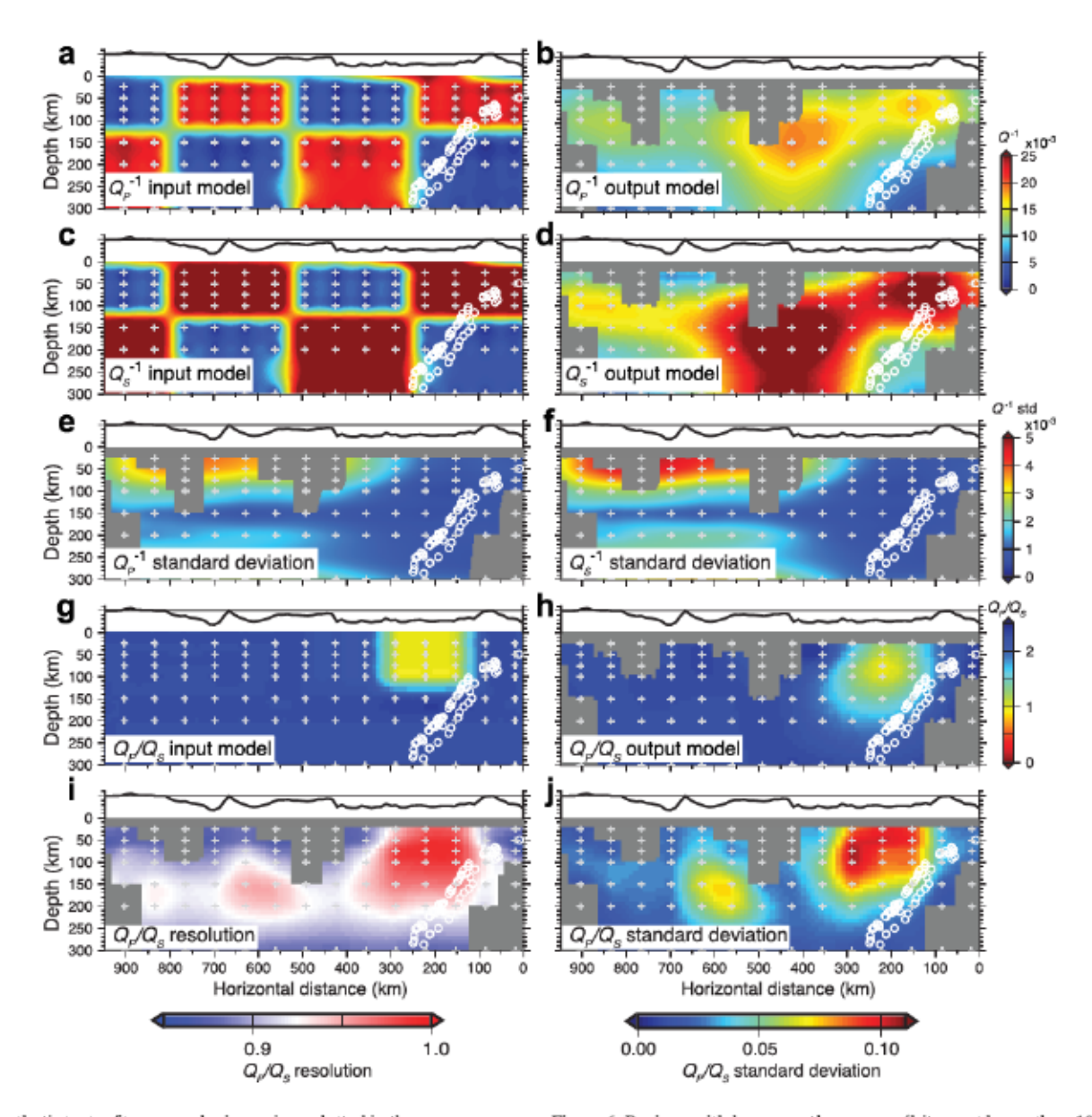


Figure 7. Synthetic tests of tomography inversions plotted in the same manner as Figure 6. Regions with low raypath coverage (hit count lower than 10) are masked with gray. (a) Checkerboard input model of  $Q_P^{-1}$ . (b) Checkerboard output model of  $Q_P^{-1}$ . (c) Checkerboard input model of  $Q_S^{-1}$ . (d) Checkerboard output model of  $Q_S^{-1}$ . (e) Standard deviation of  $Q_S^{-1}$ . (g) Synthetic input model of  $Q_P/Q_S$ . (h) Synthetic output model of  $Q_P/Q_S$ . (i) Diagonal elements of the  $Q_P/Q_S$  model resolution matrix. (j) Standard deviation of  $Q_P/Q_S$  from the SVD inversion.

The dashed curves in Figures 10a and 10b show predicted scattering  $Q_P^{-1}$  and  $Q_S^{-1}$  as functions of frequency. Parameter values of the von Kármán ACF for the upper mantle and the lithosphere are given by Mancinelli et al. (2016) and Sato et al. (2012), respectively. Measured attenuation (solid curves in Figures 10a–10c) is obtained from the tomography results in section 3 showing that  $Q_P^{-1} = 0.030$  and  $Q_S^{-1} = 0.034$  at 1 Hz beneath the Lau Basin, and the frequency dependence is fixed as  $\alpha = 0.27$ . We further calculate intrinsic attenuation (dotted curves in Figures 10a–10c) by subtracting the measured attenuation by the predicted scattering attenuation. The corresponding  $Q_P/Q_S$  ratios for scattering, measured, and intrinsic attenuation are plotted as functions of frequency in Figures 10d and 10e.

After correction for scattering attenuation, intrinsic  $Q_P/Q_S$  ratios should be higher than the measured ratios. However, since scattering attenuation in the upper mantle is negligible compared to the measured attenuation (Figure 10a), scattering has little influence on  $Q_P/Q_S$  ratios (Figure 10d). If the Tonga mantle wedge is as

WEI AND WIENS 11 of 16

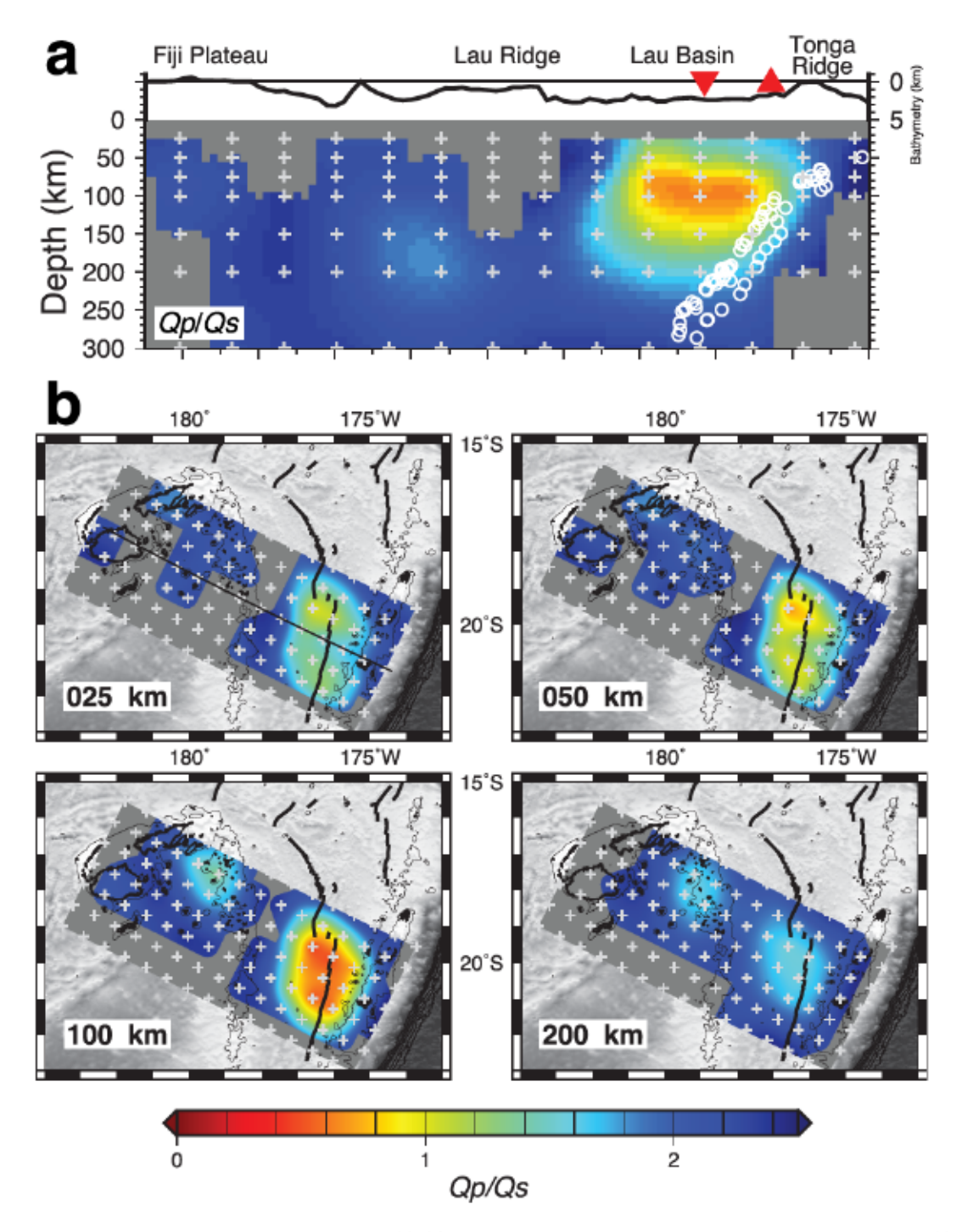


Figure 8.  $Q_{P}/Q_{S}$  tomography results obtained by inverting equation (7). (a) A  $Q_{P}/Q_{S}$  cross-section plotted in the same manner as Figure 6. (b) Maps of  $Q_{P}/Q_{S}$  at various depth. The gray box illustrates the region being inverted, whereas the light gray crosses indicate the tomography nodes. Coastlines, bathymetry, and spreading centers are plotted in the same manner as Figure 5.

heterogeneous as the lithosphere, which is unlikely, scattering can have a noticeable influence on the  $Q_P/Q_S$  ratio, but the ratio is still less than 1.5, implying significant bulk attenuation (Figure 10e). Only if we assume unrealistic values for the parameters (e.g., a=50 km and  $\varepsilon=25\%$ ) can the intrinsic  $Q_P/Q_S$  ratio be elevated to >2.25 at 1 Hz as required for no bulk attenuation (Figure 10f). Therefore, it is safe to conclude that our results primarily reflect intrinsic attenuation and  $Q_P/Q_S$  in the Tonga-Lau mantle wedge.

WEI AND WIENS 12 of 16

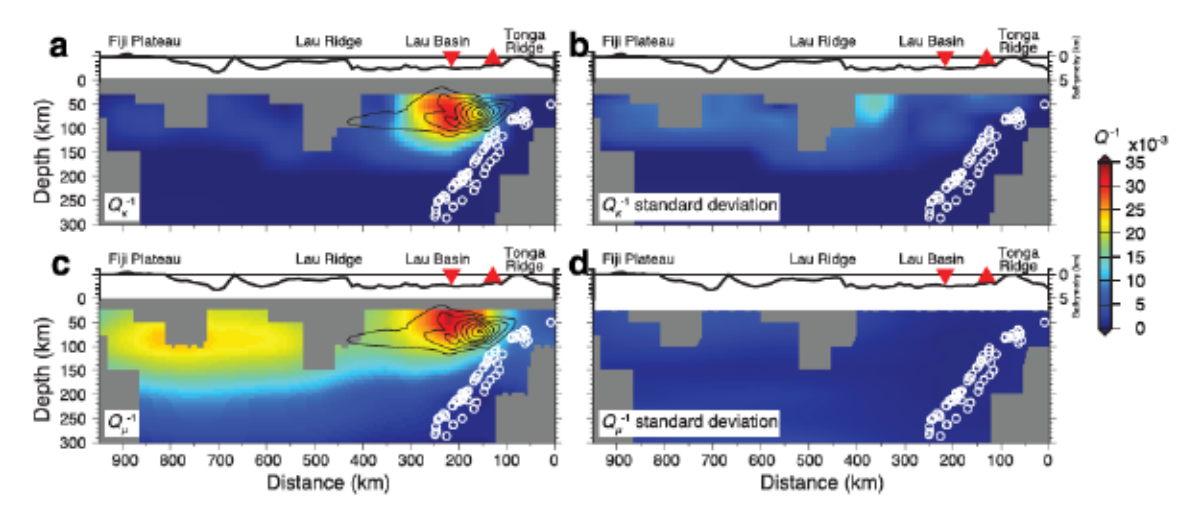


Figure 9. Tomography models showing the distribution of bulk attenuation and shear attenuation. (a) Cross section of bulk attenuation  $Q_{\kappa}^{-1}$  calculated from the  $Q_P/Q_S$  model in Figure 8 and the  $Q_P^{-1}$  model in Figure 6a. The location of the cross section is shown as the straight line in Figure 1. The black contours show the local melt production rate modeled by Wei et al. (2016), starting from 1%/Myr with a 2%/Myr increment. Other features are plotted in the same manner as Figure 8a. (b) Standard deviation of  $Q_{\kappa}^{-1}$  estimated by assuming an error of 0.2 in  $V_P/V_S$ . (c) Cross section of shear attenuation  $Q_{\mu}^{-1}$ , which is identical to the  $Q_S^{-1}$  model in Figure 6b. (d) Standard deviation of  $Q_{\mu}^{-1}$ , which is identical to Figure 7f but with a different color scale.

#### 4.2. Shear Attenuation and Arc/Back-Arc Melting

Strong anomalies of high P- and S-wave attenuation are imaged beneath the Lau Basin (Figure 6), indicating perhaps the highest shear attenuation ( $Q_{\mu}^{-1}=0.047\pm0.001$ ) known in the mantle (Figure 9b). The high shear attenuation anomalies coincide with low-velocity anomalies in the uppermost mantle wedge revealed by previous tomography work (Conder & Wiens, 2006; Wei et al., 2016; Wiens et al., 2008), suggesting high mantle temperature as well as the existence of partial melts. Hot materials of the Australian mantle upwell from the west along the mantle wedge corner flow pattern, triggering extensive decompression melting that generates a large amount of magma erupting at the back-arc spreading centers. The high shear attenuation may indicate more than 4% melt fraction in the mantle wedge according to a model by Abers et al. (2014), although more recent experiments of rock physics suggest that this melt fraction may be overestimated (Takei, 2017; Yamauchi & Takei, 2016). Partial melting in the Tonga-Lau mantle wedge is controlled by interactions between decompression melting beneath the back-arc spreading centers and flux melting beneath the arc, in which the water released from the slab plays an important role (Arai & Dunn, 2014; Dunn & Martinez, 2011; Martinez & Taylor, 2002; Wei et al., 2015).

The Tonga fore-arc is characterized by low shear attenuation, in agreement with previous attenuation studies in other subduction zones (e.g., Rychert et al., 2008; Stachnik et al., 2004). The currently active Tofua arc marks a sharp boundary that divides the low attenuation fore-arc and the high attenuation back-arc. Readers are referred to higher-resolution tomography results of SV-velocity and P-wave attenuation (Wei et al., 2016; Wei & Wiens, 2018) for details of melt distribution and mantle wedge dynamics.

#### 4.3. Bulk Attenuation and Possible Mechanisms

The extremely low  $Q_P/Q_S$  ratios and the inferred significant bulk attenuation in the mantle wedge are surprising because there is no well-characterized physical mechanism for bulk attenuation in the mantle (Faul & Jackson, 2015). Budiansky and O'Connell (1980) suggested that elastic heterogeneity and porous flow in partial melt might cause significant bulk attenuation in the upper mantle. In particular, the latter mechanism involving partial melt can potentially increase  $Q_\mu/Q_\kappa$  to 0.5 for a saturated porous solid with cracks (density = 0.1) interconnected with spherical pores (volume concentration = 5%) at frequencies above the characteristic frequency of the porous flow. Schmeling (1985) further proposed that bulk attenuation could be increased to the same order of magnitude as shear attenuation under certain conditions of complex melt geometries as a combination of ellipsoidal inclusions, thin films, and tubes. It is the combination of melt geometries rather than the melt porosity that significantly changes the  $Q_\mu/Q_\kappa$  ratio. Based on these arguments, Durek and Ekström (1995) attributed their observation of  $Q_\mu/Q_\kappa = 0.3$  within the asthenosphere to partial melt. Thermoelastic relaxation of polycrystalline aggregates was also proposed to explain the

WEI AND WIENS 13 of 16

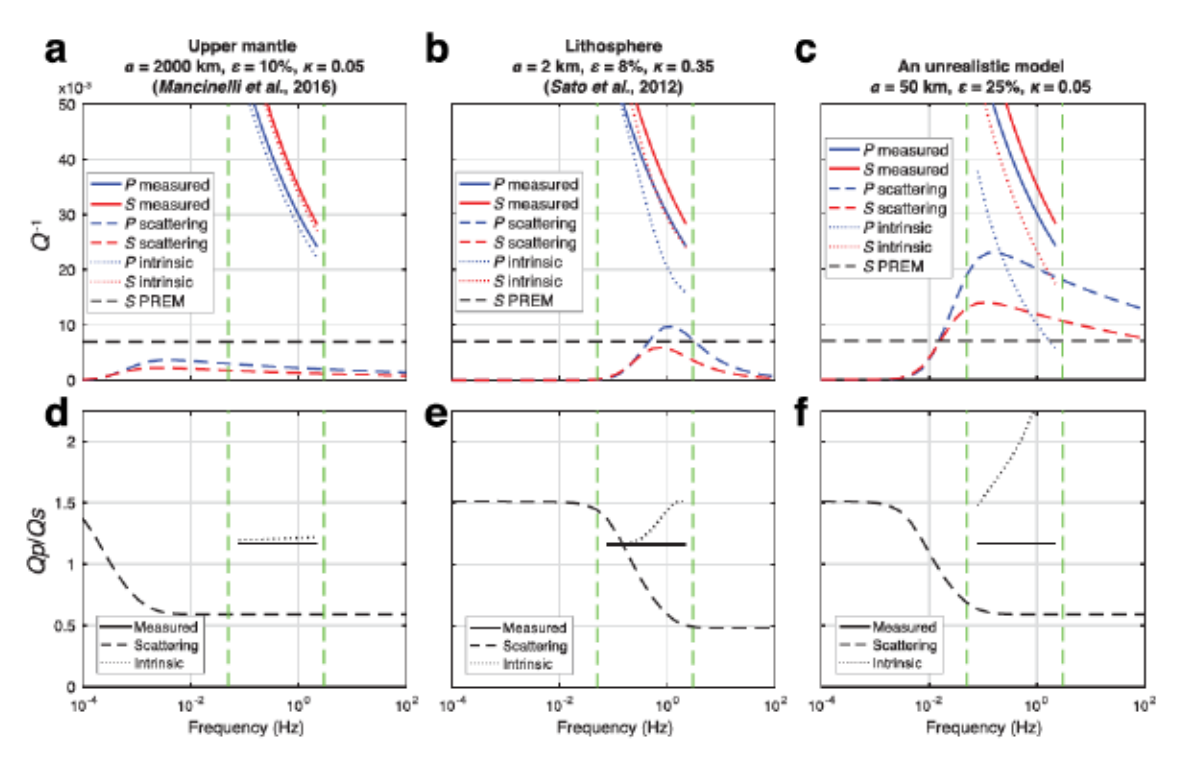


Figure 10. Effects of seismic scattering on  $Q^{-1}$  and  $Q_P/Q_S$ . Scattering attenuation is calculated based on media heterogeneity, and intrinsic attenuation is obtained by subtracting scattering attenuation from measured attenuation. Media heterogeneity is statistically parameterized by a von Kármán autocorrelation function. (a and d)  $Q^{-1}$  and  $Q_P/Q_S$  for the upper mantle calculated from Mancinelli et al. (2016). (b and e)  $Q^{-1}$  and  $Q_P/Q_S$  for the lithosphere calculated from Sato et al. (2012). (c and f)  $Q^{-1}$  and  $Q_P/Q_S$  calculated for a model with unrealistic parameters for the upper mantle, whose corresponding intrinsic  $Q_P/Q_S$  can be elevated to >2.25 at 1 Hz. In the top panels, the blue and red curves indicate P- and P- and

potential bulk attenuation in the lower mantle (Budiansky et al., 1983). Recently, Li and Weidner (2008) suggested that the stress perturbation of seismic waves can soften bulk modulus, that is, increase bulk attenuation, through a loop of solid-solid phase transitions from olivine to ringwoodite in the mantle transition zone on a timescale of 100 s. Furthermore, Li and Weidner (2013) suggested that when seismic waves travel though a partially molten region, the stress perturbation will change melt fraction through a solid-liquid phase change and thus cause bulk attenuation.

The high bulk attenuation anomalies beneath the Lau Basin coincide with the location where extensive partial melting is both expected (Kelley et al., 2006) and indicated by the seismic velocity structure (Wei et al., 2015; Wiens et al., 2008), thus favoring the mechanisms involving partial melt (Budiansky & O'Connell, 1980; Li & Weidner, 2013; Schmeling, 1985).

We observe significant bulk attenuation  $Q_{\kappa}^{-1}$  as high as  $0.037 \pm 0.008$ , and a  $Q_{\mu}/Q_{\kappa}$  ratio of about 0.75 beneath the Lau back-arc spreading centers. By comparison, Durek and Ekström (1995) found  $Q_{\kappa}^{-1} = 4.7 \times 10^{-3}$  and a  $Q_{\mu}/Q_{\kappa}$  ratio of 0.3 within the global asthenosphere, and a later inversion of a larger dataset found  $Q_{\kappa}^{-1} = 1.1 \times 10^{-3}$  corresponding to a  $Q_{\mu}/Q_{\kappa}$  ratio of 0.13 (Durek & Ekström, 1996). It seems likely that bulk attenuation inferred at asthenospheric depths in global models (Durek & Ekström, 1995, 1996) may result from absorption within localized regions of extensive partial melting such as beneath the Lau Basin and mid-ocean ridges (MORs), which make only a small part of the asthenosphere. If we assume that there are approximately eight magmatic regions with extensive mantle partial melt in the world similar to the Lau Basin in terms of  $Q_{\kappa}$  value and size, and if the bulk attenuation of MOR asthenosphere is about half of that of the Lau Basin uppermost mantle (i.e.  $Q_{\kappa}^{-1}$  of 0.01 encompassing a 600-km-wide region along all MORs), the global asthenosphere  $Q_{\kappa}^{-1}$  value of  $1.1 \times 10^{-3}$  obtained by Durek and Ekström (1996) can be explained as a geometric average of these high-bulk-attenuation regions.

WEI AND WIENS 14 of 16



Unfortunately, the lack of experimental constraints on bulk attenuation renders it difficult to associate the observed bulk attenuation with a particular relaxation mechanism or to interpret the results quantitatively. However, the Lau Basin observations suggest that extensive regions of partial melting in the upper mantle are associated with significant bulk attenuation and provide a potential solution for the long-standing debate about the location and magnitude of bulk attenuation in the Earth's interior. We hope that this strong evidence of the association of bulk attenuation and melting will inspire more theoretical and experimental investigations of this phenomenon.

#### 5. Conclusions

By analyzing the spectral decay of P and S waves in the Tonga-Lau subduction system, we observe unusually low  $Q_P/Q_S$  ratios in the mantle wedge. This indicates significant intrinsic bulk attenuation, with  $Q_\kappa^{-1}$  as great as 0.037  $\pm$  0.008 and a ratio of bulk to shear attenuation  $Q_\mu/Q_\kappa$  of ~0.75. The high bulk attenuation is observed immediately beneath the Lau back-arc spreading centers, where extensive partial melting occurs. We thus propose that the bulk attenuation is caused by one or more mechanisms related to partial melt, including porous melt flow through interconnected pores and incremental stress-induced changes in melt fraction. However, these mechanisms have not been well understood in theory or characterized by laboratory experiments. The observation of bulk attenuation in upper mantle melting regions can explain previous observations of bulk attenuation in the earth. More measurements of the bulk attenuation beneath MORs and other specific mantle regions subject to partial melting, as well as more experimental rock physics work, are needed to better characterize the effects of melt on seismic bulk attenuation.

## Acknowledgments References

We thank Guy Masters, Peter M.

Shearer, Catherine Rychert, Yasuko

Takei, Ian Jackson, and Zachary Eilon

for their helpful discussions, Nicholas

Mancinelli shared his computer codes

and provided constructive comments

appreciate the associate editor and two

on scattering attenuation. We also

anonymous reviewers who provide

PASSCAL instrument center and the

Woods Hole Oceanographic Institution

Observatory OBSIP facilities provided

Foundation grants OCE-0426408 (the

the land and OBS instrumentation.

respectively. This work was made

RIDGE2000 program to D. A. W.),

EAR-0911137 (D. A. W.), and OCE-

supported by Michigan State University

Geology Alumni Endowment and the

Cecil H. and Ida M. Green Foundation.

Raw seismic data are available at Data

Management Center of Incorporated

Research Institutions for Seismology

network IDs YL and Z1. The

t\*, and tomography models are

Collaboration (EMC) named as

10.17611/dp/tonga2019.

available at the IRIS Earth Model

TongaLau.Q.2019: https://doi.org/

(www.iris.edu/dms/nodes/dmc), under

earthquake catalog, measurements of

1842989 (S. S. W.). S. S. W. is also

constructive comments. The IRIS-

and Lamont-Doherty Earth

possible by National Science

Abers, G. A., Fischer, K. M., Hirth, G., Wiens, D. A., Plank, T., Holtzman, B. K., et al. (2014). Reconciling mantle attenuation-temperature relationships from seismology, petrology, and laboratory measurements. Geochemistry, Geophysics, Geosystems, 15, 3521–3542. https://doi.org/10.1002/2014GC005444

Anderson, D. L., & Given, J. W. (1982). Absorption band Q model for the Earth. Journal of Geophysical Research, 87(B5), 3893–3904. https://doi.org/10.1029/JB087iB05p03893

Anderson, D. L., & Hart, R. S. (1978). Q of the Earth. Journal of Geophysical Research, 83(B12), 5869–5882. https://doi.org/10.1029/ JB083iB12p05869

Anderson, J. G., & Hough, S. E. (1984). A model for the shape of the Fourier amplitude spectrum of acceleration at high frequencies. Bulletin of Seismological Society of America, 74(5), 1969–1993.

Batterin of Secondogical Society of America, 74(5), 1909–1993.
Arai, R., & Dunn, R. A. (2014). Seismological study of Lau back arc crust: Mantle water, magmatic differentiation, and a compositionally zoned basin. Earth and Planetary Science Letters, 390, 304–317. https://doi.org/10.1016/j.epsl.2014.01.014

Barazangi, M., & Isacks, B. (1971). Lateral variations of seismic-wave attenuation in the upper mantle above the inclined earthquake zone of the Tonga Island Arc: Deep anomaly in the upper mantle. *Journal of Geophysical Research*, 76(35), 8493–8516. https://doi.org/10.1029/JB076i035p08493

Bevis, M., Taylor, F. W., Schutz, B. E., Recy, J., Isacks, B. L., Helu, S., et al. (1995). Geodetic observations of very rapid convergence and back-arc extension at the Tonga arc. Nature, 374(6519), 249–251.

Bowman, J. R. (1988). Body wave attenuation in the Tonga Subduction Zone. Journal of Geophysical Research, 93(B3), 2125–2139. https://doi.org/10.1029/JB093iB03p02125

Budiansky, B., & O'Connell, R. J. (1980). Bulk dissipation in heterogeneous media. In S. Nemat-Nasser (Ed.), Solid Earth Geophysics and Geotechnology (1–10). New York: American Society of Mechanical Engineers.

Budiansky, B., Sumner, E. E., & O'Connell, R. J. (1983). Bulk thermoelastic attenuation of composite materials. Journal of Geophysical Research, 88(B12), 10,343–10,348. https://doi.org/10.1029/JB088iB12p10343

Conder, J. A., & Wiens, D. A. (2006). Seismic structure beneath the Tonga arc and Lau back-arc basin determined from joint Vp, Vp/Vs tomography. Geochemistry, Geophysics, Geosystems, 7, Q03018. https://doi.org/10.1029/2005GC001113

Dalton, C. A., Ekström, G., & Dziewoński, A. M. (2008). The global attenuation structure of the upper mantle. *Journal of Geophysical Research*, 113, B09303. https://doi.org/10.1029/2007JB005429

Dunn, R. A., & Martinez, F. (2011). Contrasting crustal production and rapid mantle transitions beneath back-arc ridges. Nature, 469(7329), 198–202. https://doi.org/10.1038/nature09690

Durek, J. J., & Ekström, G. (1995). Evidence of bulk attenuation in the asthenosphere from recordings of the Bolivia Earthquake. Geophysical Research Letters, 22(16), 2309–2312. https://doi.org/10.1029/95GL01434

Durek, J. J., & Ekström, G. (1996). A radial model of anelasticity consistent with long-period surface-wave attenuation. Bulletin of Scismological Society of America, 86(1A), 144–158.

Dziewoński, A. M., & Anderson, D. L. (1981). Preliminary reference Earth model. Physics of the Earth and Planetary Interiors, 25(4), 297–356. https://doi.org/10.1016/0031-9201(81)90046-7

Eilon, Z. C., & Abers, G. A. (2017). High seismic attenuation at a mid-ocean ridge reveals the distribution of deep melt. Science Advances, 3(5), e1602829. https://doi.org/10.1126/sciadv.1602829

Faul, U., & Jackson, I. (2015). Transient creep and strain energy dissipation: An experimental perspective. Annual Review of Earth and Planetary Sciences, 43(1), 541–569. https://doi.org/10.1146/annurev-earth-060313-054732

Flanagan, M. P., & Wiens, D. A. (1998). Attenuation of broadband P and S waves in Tonga: Observations of frequency dependent Q. Pure and Applied Geophysics, 153(2-4), 345–375. https://doi.org/10.1007/s000240050199

WEI AND WIENS 15 of 16



- Gung, Y., & Romanowicz, B. (2004). Q tomography of the upper mantle using three-component long-period waveforms. Geophysical Journal International, 157(2), 813–830. https://doi.org/10.1111/j.1365-246X.2004.02265.x
- Hauksson, E., & Shearer, P. M. (2006). Attenuation models (Q<sub>P</sub> and Q<sub>S</sub>) in three dimensions of the southern California crust: Inferred fluid saturation at seismogenic depths. Journal of Geophysical Research, 111, B05302. https://doi.org/10.1029/2005JB003947
- Jackson, I. (2015). Properties of rocks and minerals: Physical origins of anelasticity and attenuation in rock. In G. Schubert (Ed.), Treatise on Geophysics, (Second ed.pp. 539–571). Oxford: Elsevier.
- Karato, S.-L. (1993). Importance of anelasticity in the interpretation of seismic tomography. Geophysical Research Letters, 20(15), 1623–1626. https://doi.org/10.1029/93GL01767
- Kelley, K. A., Plank, T., Grove, T. L., Stolper, E. M., Newman, S., & Hauri, E. (2006). Mantle melting as a function of water content beneath back-arc basins. Journal of Geophysical Research, 111, B09208. https://doi.org/10.1029/2005JB003732
- Lees, J. M., & Park, J. (1995). Multiple-taper spectral analysis: A stand-alone C-subroutine. Computers & Geosciences, 21(2), 199–236. https://doi.org/10.1016/0098-3004(94)00067-5
- Li, L., & Weidner, D. J. (2008). Effect of phase transitions on compressional-wave velocities in the Earth's mantle. Nature, 454(7207), 984–986. https://doi.org/10.1038/nature07230
- Li, L., & Weidner, D. J. (2013). Effect of dynamic melting on acoustic velocities in a partially molten peridotite. Physics of the Earth and Planetary Interiors, 222, 1–7. https://doi.org/10.1016/j.pepi.2013.06.009
- Madariaga, R. (1976). Dynamics of an expanding circular fault. Bulletin of Seismological Society of America, 66(3), 639-666.
- Mancinelli, N., Shearer, P., & Liu, Q. (2016). Constraints on the heterogeneity spectrum of Earth's upper mantle. Journal of Geophysical Research: Solid Earth, 121, 3703–3721. https://doi.org/10.1002/2015JB012641
- Martinez, F., & Taylor, B. (2002). Mantle wedge control on back-arc crustal accretion. Nature, 416(6879), 417–420. https://doi.org/10.1038/ 4164179
- Menke, W. (2012). Chapter 7 Applications of vector spaces. In W. Menke (Ed.), Geophysical data analysis: Discrete inverse theory, (Third ed. pp. 123–148). Boston: Academic Press.
- Menke, W. (2014). Review of the generalized least squares method. Surveys in Geophysics, 36(1), 1–25. https://doi.org/10.1007/s10712-014-9303-1
- Nakajima, J., Hada, S., Hayami, E., Uchida, N., Hasegawa, A., Yoshioka, S., et al. (2013). Seismic attenuation beneath northeastern Japan: Constraints on mantle dynamics and arc magmatism. *Journal of Geophysical Research: Solid Earth*, 118, 5838–5855. https://doi.org/ 10.1002/2013JB010388
- Pozgay, S. H., Wiens, D. A., Conder, J. A., Shiobara, H., & Sugioka, H. (2009). Seismic attenuation tomography of the Mariana subduction system: Implications for thermal structure, volatile distribution, and slow spreading dynamics. Geochemistry, Geophysics, Geosystems, 10, QQ4X05. https://doi.org/10.1029/2008GC002313
- Resovsky, J., Trampert, J., & Van der Hilst, R. D. (2005). Error bars for the global seismic Q profile. Earth and Planetary Science Letters, 230(3-4), 413-423. https://doi.org/10.1016/j.epsl.2004.12.008
- Romanowicz, B. A., & Mitchell, B. J. (2015). Deep Earth structure: Q of the Earth from crust to core. In G. Schubert (Ed.), Treatise on geophysics, (Second ed.pp. 789–827). Oxford: Elsevier.
- Roth, E. G., Wiens, D. A., Dorman, L. M., Hildebrand, J., & Webb, S. C. (1999). Seismic attenuation tomography of the Tonga-Fiji region using phase pair methods. *Journal of Geophysical Research*, 104(B3), 4795–4809. https://doi.org/10.1029/1998JB900052
- Rychert, C. A., Fischer, K. M., Abers, G. A., Plank, T., Syracuse, E., Protti, J. M., et al. (2008). Strong along-arc variations in attenuation in the mantle wedge beneath Costa Rica and Nicaragua. Geochemistry, Geophysics, Geosystems, 9, Q10S10. https://doi.org/10.1029/2008GC002040
- Sailor, R. V., & Dziewonski, A. M. (1978). Measurements and interpretation of normal mode attenuation. Geophysical Journal of the Royal Astronomical Society, 53(3), 559–581. https://doi.org/10.1111/j.1365-246X.1978.tb03760.x
- Sato, H. (1984). Attenuation and envelope formation of three-component seismograms of small local earthquakes in randomly inhomogeneous lithosphere. Journal of Geophysical Research, 89(B2), 1221–1241. https://doi.org/10.1029/JB089iB02p01221
- Sato, H. (1990). Unified approach to amplitude attenuation and coda excitation in the randomly inhomogeneous lithosphere. Pure and Applied Geophysics, 132(1-2), 93–121. https://doi.org/10.1007/bf00874359
- Sato, H., Fehler, M. C., & Maeda, T. (2012). Seismic wave propagation and scattering in the heterogeneous earth, (2nd ed.pp. 160–180). Berlin: Springer.
- Schmeling, H. (1985). Numerical models on the influence of partial melt on elastic, anelastic and electric properties of rocks. Part I: elasticity and anelasticity. Physics of the Earth and Planetary Interiors, 4I(1), 34–57. https://doi.org/10.1016/0031-9201(85)90100-1
- Stachnik, J. C., Abers, G. A., & Christensen, D. H. (2004). Seismic attenuation and mantle wedge temperatures in the Alaska subduction zone. Journal of Geophysical Research, 109, B10304. https://doi.org/10.1029/2004JB003018
- Takei, Y. (2017). Effects of partial melting on seismic velocity and attenuation: A new insight from experiments. Annual Review of Earth and Planetary Sciences, 45(1), 447–470. https://doi.org/10.1146/annurev-earth-063016-015820
- Um, J., & Thurber, C. (1987). A fast algorithm for two-point seismic ray tracing. Bulletin of Seismological Society of America, 77(3), 972–986.
  Wei, S. S., & Wiens, D. A. (2018). P-wave attenuation structure of the Lau back-arc basin and implications for mantle wedge processes.
  Earth and Planetary Science Letters, 502, 187–199. https://doi.org/10.1016/j.epsl.2018.09.005
- Wei, S. S., Wiens, D. A., van Keken, P. E., & Cai, C. (2017). Slab temperature controls on the Tonga double seismic zone and slab mantle dehydration. Science Advances, 3(1). https://doi.org/10.1126/sciadv.1601755
- Wei, S. S., Wiens, D. A., Zha, Y., Plank, T., Webb, S. C., Blackman, D. K., et al. (2015). Seismic evidence of effects of water on melt transport in the Lau back-arc mantle. Nature, 518(7539), 395–398. https://doi.org/10.1038/nature14113
- Wei, S. S., Zha, Y., Shen, W., Wiens, D. A., Conder, J. A., & Webb, S. C. (2016). Upper mantle structure of the Tonga-Lau-Fiji region from Rayleigh wave tomography. Geochemistry, Geophysics, Geosystems, 17, 4705–4724. https://doi.org/10.1002/2016GC006656
- Wiens, D. A., Conder, J. A., & Faul, U. H. (2008). The seismic structure and dynamics of the mantle wedge. Annual Review of Earth and Planetary Sciences, 36(1), 421–455. https://doi.org/10.1146/annurev.earth.33.092203.122633
- Yamauchi, H., & Takei, Y. (2016). Polycrystal anelasticity at near-solidus temperatures. Journal of Geophysical Research Solid Earth, 121, 7790–7820. https://doi.org/10.1002/2016JB013316
- Yang, Y., Forsyth, D. W., & Weeraratne, D. S. (2007). Seismic attenuation near the East Pacific Rise and the origin of the low-velocity zone. Earth and Planetary Science Letters, 258(1-2), 260-268. https://doi.org/10.1016/j.epsl.2007.03.040
- Zha, Y., Webb, S. C., & Menke, W. (2013). Determining the orientations of ocean bottom seismometers using ambient noise correlation. Geophysical Research Letters, 40, 3585–3590. https://doi.org/10.1002/grl.50698

WEI AND WIENS 16 of 16